processes

MDPI

Article

Modeling of Tar Removal in a Partial Oxidation Burner: Effect of Air Injection on Temperature, Tar Conversion, and Soot Formation

Yongbin Wang [1,2], Guoqiang Cao [1,*], Sen Wang [1,2], Donghai Hu [1], Zhongren Ba [1], Chunyu Li [1], Jiantao Zhao [1,*] and Yitian Fang [1]

[1] State Key Laboratory of Coal Conversion, Institute of Coal Chemistry, Chinese Academy of Sciences, Taiyuan 030001, China
[2] University of Chinese Academy of Sciences, Beijing 100049, China
* Correspondence: caoguoqiang@sxicc.ac.cn (G.C.); zhaojt@sxicc.ac.cn (J.Z.)

Abstract

In this study, a three-dimensional computational fluid dynamic (CFD) model was constructed and validated against experimental data. The oxygen injection methods—specifically the primary air flow and secondary air flow—were investigated. The results demonstrate that primary air flow is the dominant factor in combustion. An increase of primary air from an φ of 0.20 to 0.75 lead to a rise in combustion peak temperature from 892.17 K to 1321.02 K, while simultaneously expending the flame combustion zone and enhancing the conversion of $C_{10}H_8$ and CH_4. Conversely, increasing the secondary air flow from 1 L/min to 7 L/min reduced the centrally measured temperatures form 886.09 K to 856.07 K due to irregular flow patterns, which expanded the central low-temperature region. While secondary air flow promoted more uniform reactant conversion and slightly suppressed intermediate products (e.g., soot, C_6H_6), its overall effect was secondary to that of the primary air. This research reveals a critical design insight: using primary air injection to introduce oxygen into the reactor is a reasonable approach. The findings provide valuable guidance for optimizing partial oxidation burner design and operating conditions to maximize tar conversion while maintaining reactor integrity. The study also establishes a rigorously validated CFD framework for analyzing complex reacting flows in tar thermochemical conversion reactors.

Keywords: biomass gasification producer gas; partial oxidation burner; combustion modeling; tar conversion; soot formation

check for updates

Academic Editors: Carmen Branca and Antonio Galgano

Received: 30 October 2025
Revised: 26 November 2025
Accepted: 26 November 2025
Published: 3 December 2025

Citation: Wang, Y.; Cao, G.; Wang, S.; Hu, D.; Ba, Z.; Li, C.; Zhao, J.; Fang, Y. Modeling of Tar Removal in a Partial Oxidation Burner: Effect of Air Injection on Temperature, Tar Conversion, and Soot Formation. *Processes* **2025**, *13*, 3903. https://doi.org/10.3390/pr13123903

Copyright: © 2025 by the authors. Licensee MDPI, Basel, Switzerland. This article is an open access article distributed under the terms and conditions of the Creative Commons Attribution (CC BY) license (https://creativecommons.org/licenses/by/4.0/).

1. Introduction

Amid escalating challenges in energy security and intensifying global climate instability, there is a growing imperative to develop and utilize renewable energy [1,2]. Biomass gasification, a thermochemical process that converts biomass into syngas—a mixture of carbon monoxide (CO) and hydrogen (H_2)—offers significant potential due to its high energy efficiency, adaptability to diverse feedstocks, and operational flexibility [3,4]. The primary product of this process, producer gas, contains syngas, methane (CH_4), carbon dioxide (CO_2), water (H_2O), and minor hydrocarbons, serving as a precursor for various downstream energy conversion processes [5]. Although biomass pretreatment can alter the characteristics and yield of gasification tar [6,7], gasification tar is also influenced by

parameters such as gasifying agent [8] and reaction temperature [9]. Therefore, the purification of producer gas remains a significant challenge that hinders its commercialization and broader adoption [10,11].

Various methods for the purification of producer gas have been developed and are primarily categorized into three main types: (i) non-catalytic reforming, which converts tar in a gaseous mixture primarily composed of syngas and gaseous hydrocarbons [12,13]; (ii) catalytic cracking, which decomposes tar and light hydrocarbons into H_2 and CO [3,14]; and (iii) mechanical removal of tar from producer gas using mechanical devices [15]. The majority of research on producer gas purification has focused on catalytic cracking due to its high energy efficiency and carbon conversion rate [3,6]. Meanwhile, due to its simplicity and maturity, mechanical removal remains the most widely adopted method in industrial applications. However, both catalytic and mechanical methods face limitations such as short catalyst lifespans, low carbon conversion rates, and significant secondary pollution, which have spurred increasing interest in non-catalytic reforming [16–18].

The dominant strategy in non-catalytic reforming involves the introduction of oxygen to enhance the temperature of producer gas, thereby accelerating the cracking of tar. As highlighted by Hoeven et al. [19], oxygen functions as a critical free radical initiator, playing a pivotal role in the initiation of chain reactions and subsequent chemical processes. Oxygen also facilitates exothermic reactions within the producer gas, generating the thermal energy required for further reactions. However, excessive oxygen can lead to the formation of excessive polycyclic aromatic hydrocarbons (PAHs) and even soot [20]. Conversely, hydrogen addition has been shown to suppress PAH and soot formation [21,22], while steam has minimal impact on tar conversion [22,23]. Research indicates that simple aromatics such as naphthalene can form heavier PAHs at elevated temperatures [24], and inlet tar undergoes polymerization/sooting mechanisms to yield soot [23]. Thermal cracking achieves 90% tar reduction at 1473.15 K.

According to the research by Wu et al., the maximum reduction in tar content within pyrolysis vapors is achieved at 1173.15 K with an φ of 0.34. However, elevated φ values lead to over-combustion of non-condensable gases such as H_2, CO, and CH_4, resulting in reduced gas yields [20,25]. For biomass gasification producer gas, a 90% tar reduction is observed at an φ of 0.20 [21]. Houben et al. investigated tar reduction dynamics using a partial oxidation burner with naphthalene introduced into synthetic producer gas, confirming optimal reduction efficacy at an φ of 0.20 [26]. Collectively, these studies indicate that the partial oxidation of biomass gasification producer gas is primarily governed by oxygen concentration and temperature.

By coupling the regulating effect of biomass pretreatment on gasification tar with the purification effect of partial oxidation on producer gas, the economics of biomass gasification can be further improved. However, little research has been conducted on the reaction mechanisms occurring inside the partial oxidation reactor for biomass gasification producer gas. In particular, there is a need for studies on the optimization of O_2 addition method on temperature distribution and tar reduction. Building upon these considerations, this study elucidates the mechanistic interplay between oxygen and producer gas within a partial oxidation reactor. By integrating CFD simulations with experimental validation, we systematically investigated how distinct oxygen injection strategies govern temperature distribution profiles and tar reduction efficiency. The findings provide foundational insights for optimizing partial oxidation reactor design and mitigating performance fluctuations in tar reforming.

2. Mathematical Model and Data Evaluation

This study simulates the partial oxidation process, which involves complex chemical reactions. To model turbulence, the realizable k-ε model is employed. This approach is combined with a combustion model and a detailed chemical kinetics mechanism, as detailed in the following sections.

2.1. Combustion Model

This study employs a hybrid computational strategy, utilizing a non-premixed combustion model for preliminary thermal mapping to mitigate computational burden, followed by implementation of the Eddy-Dissipation Concept (EDC) model to simulate intricate reaction kinetic within the partial oxidation reactor.

2.1.1. Non-Premixed Combustion Model

Given the low-Mach-number diffusion flame characteristics in the burner region of interest, the Schwab-Zeldovitch variable (Z) is adopted to characterize flame structure [27]. This conserved scalar approach is widely implemented in non-premixed combustion modeling, offering both thermodynamic insight and computational simplification through reduced-order formulation. The Schwab-Zeldovitch mixture fraction (Z) is defined as the normalized mass fraction difference between fuel and oxidizer streams:

$$Z = \frac{Y_F - Y_O}{Y_{F0} - Y_{O0}} \tag{1}$$

In this formulation, Y_F and Y_O denote the local mass fractions of fuel and oxidizer, respectively, while Y_{F0} and Y_{O0} represent their reference mass fractions in the un-burnt feed streams.

The conservation equations governing fuel (F) and oxidizer (O) mass fractions are formulated as follows:

$$\frac{\partial \rho Y_F}{\partial t} + \nabla \cdot (\rho \vec{u} Y_F) = \nabla \cdot (\rho D_F \nabla Y_F) + \omega_F \tag{2}$$

$$\frac{\partial \rho Y_O}{\partial t} + \nabla \cdot (\rho \vec{u} Y_O) = \nabla \cdot (\rho D_O \nabla Y_O) + \omega_O \tag{3}$$

where ω_F and ω_O represent the volumetric generation rates of the fuel and oxidizer, respectively. Assuming the diffusion coefficients of fuel and oxidizer are equal ($D_F = D_O$), the conservation equation for mixture fraction Z can be derived by linearly combining the aforementioned equations:

$$\frac{\partial \rho Z}{\partial t} + \nabla \cdot (\rho u Z) = \nabla \cdot (\rho D \nabla Z) \tag{4}$$

Here, Z_f denotes the critical value determined by the stoichiometric ratio, wherein the fuel and oxidizer undergo a reaction at the point $Z = Z_f$, whereas no chemical reaction occurs in regions where $Z \neq Z_f$.

2.1.2. Eddy-Dissipation Concept Model

The EDC model provides a framework for incorporating detailed chemical kinetics in turbulent combustion simulations [28]. Its fundamental premise is that chemical reactions predominantly occur within fine-scale turbulent structures, conceptualized as perfectly

mixed stirred reactors. For each computational cell, the steady-state composition within these fine scales is determined by solving:

$$\frac{dY_J^*}{dt} = \frac{w_J^*}{\overline{\rho}} + \frac{Y_J^0 - Y_J^*}{\tau^*} \tag{5}$$

$$\widetilde{Y}_J = \xi^{*3} Y_J^* + (1.0 - \xi^{*3}) Y_J^0 \tag{6}$$

where $\widetilde{Y}_J$ mean mass fraction of species J, while Y_J^* and Y_J^0 denote the mass fractions of fine scales and surrounding gas, respectively. The time variable is denoted as t, and w_J^* signifies the reaction rate within the fine scales. The characteristic length ξ^* of the fine scales can be determined by the following formula:

$$\xi^* = C_\xi \left(\frac{\mu\varepsilon}{\overline{\rho}k^2}\right)^{1/4} \tag{7}$$

where C_ξ is volume fraction constant, set as 2.1377; μ denotes the viscosity; ε is turbulent dissipation rate, and k denotes the turbulent kinetic energy. Species are assumed to react in the fine scales over s time scale

$$\tau^* = C_\tau \left(\frac{\mu}{\overline{\rho}\varepsilon}\right)^{1/2} \tag{8}$$

where C_ξ is fine scales residence time, and C_τ is time scale constant equal to 0.4082.

The mean reaction rate of chemical species J is computed as:

$$\overline{w}_J = \frac{\rho\xi^{*2}}{\tau * (1 - \xi^{*3})} (Y_J^* - \widetilde{Y}_J) \tag{9}$$

The Damköhler number is an important parameter that compares chemical reaction time with turbulent mixing time. For computational cases considering detailed chemical reactions, the Damköhler number can be calculated using the following formula:

$$Da = \left(\frac{\nu c_r^2}{\varepsilon}\right)^{1/2} \tag{10}$$

where c_r is the Arrhenius net rate of reaction/ρ, ν is the kinematic viscosity, ε is the local dissipation rate of turbulent kinetic energy, and ρ is the local mixture density. After analysis, the Damköhler number for key reactions in this study's conditions ranges from 0.9 to 10.3. This demonstrates that selecting the EDC model to simulate this experimental condition is a relatively appropriate choice.

2.2. Kinetic Model

In this study, a detailed kinetic mechanism model was employed to describes biomass tar conversion process. The mechanism integrates gas-phase pyrolysis and oxidation with a kinetic model for soot nucleation and growth, demonstrating superior predictive capability for tar reforming processes accompanied by soot formation. In model validation, the kinetic mechanism model could effectively capture species concentration variations and temperature-dependent trends for tar reaction. To enhance computational efficiency, a strategically reduced version of the mechanism—containing 68 species and 679 elementary reactions—was applied for simulating tar conversion. This reduction was achieved by eliminating extraneous species and reactions, while retaining solver compatibility for chemical reaction simulations.

The kinetic model incorporates the principal species participating in the tar conversion process. These comprise: light gas components such as O_2, H_2, CO, CO_2, H_2O, CH_4, C_2H_2, C_2H_4, C_2H_6, C_3H_4, C_3H_6, C_3H_8, etc.; tar components including 2,4-Cyclopentadiene-1-one (denoted as C_5H_4O in the kinetic model file), Phenol (C_6H_5OH), Benzene (C_6H_6), Toluene (C_7H_8), Naphthalene ($C_{10}H_8$), Phenanthrene (A3), Benzanthracene (A4), Indene (INDENE), etc.; and soot components like BIN1A, BIN1B, BIN5A, BIN5B, etc. In particular, for biomass gasification tar, the following model compounds can act as representatives owing to their distinct reactivity: Benzene (C_6H_6) for primary tar, Naphthalene ($C_{10}H_8$) for tertiary tar, Phenol (C_6H_5OH) for phenolic tar constituents, and 2,4-Cyclopentadiene-1-one (C_5H_4O) for other oxygen-containing species [15]. In simulations, the content of these four model tar compounds can be tailored to the actual tar composition, allowing theoretical simulation of all biomass gasification tar types.

2.3. Data Evaluation

The reactor performance was evaluated in terms of the tar conversion efficiency, η_{tar} (%), and the soot yield, Y_{soot} (%). η_{tar} was calculated using the following equation:

$$\eta_{tar} = \frac{\dot{m}_{tar,initial} - \dot{m}_{tar,out}}{\dot{m}_{tar,initial}} \times 100\% \quad (11)$$

where $\dot{m}_{tar,initial}$ is the initial tar mass flow rate, g/min. $\dot{m}_{tar,out}$ is the outlet tar mass flow rate, g/min.

Soot yield is defined as the ratio of soot mass to the total fuel mass, and can be calculated by the following equation:

$$Y_{soot} = \frac{\dot{m}_{soot,out}}{\dot{m}_{fuel,initial}} \times 100\% \quad (12)$$

where $\dot{m}_{soot}$ is the soot mass flow rate, g/min; $\dot{m}_{fuel,initial}$ is the initial fuel mass flow rate, g/min.

3. Introduction of Research Objectives and Grid Validation

3.1. Introduction of the Combustion Equipment

Figure 1 shows the Schematic view of the reactor system and the injection nozzles. The experimental apparatus, constructed from stainless steel, is enclosed within a 750 mm tall, 150 mm diameter glass bell (Figure 1a) to regulate the burner's air intake. The tar enters the burner at the bottom of the central inner tube and flows into the reactor. Approximately 50 mm downstream, it meets the primary air, which is injected through seven injection nozzles into the inner tubes. Secondary air is introduced into the reactor via the secondary air inlet on the burner's base and reacts with the remaining tar to undergo partial oxidation, detailed descriptions of the equipment are provided in the previous literature [26].

The introduced air is bifurcated into two distinct streams: primary air flow and secondary air flow. The primary air, serving as a combustion-supporting medium, is injected through seven inclined nozzles into the reactor, as shown in Figure 1b. Characterized by a higher volume flow rate and faster injection, it facilitates the formation of a stable and intense flame. In contrast, secondary air functions as a supplementary air supply, typically introduced after combustion initiation, with a smaller volume flow rate and slower injection into the reactor, primarily providing limited oxygen for partial oxidation of tar components.

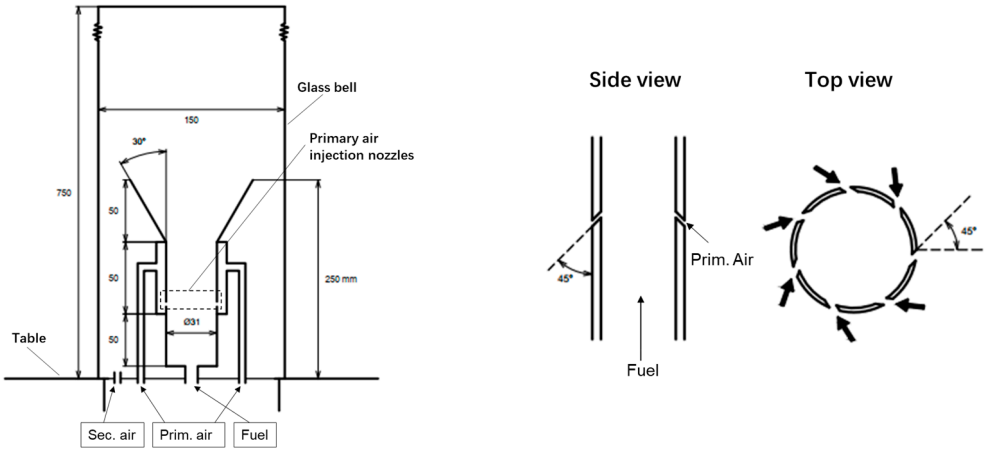


Figure 1. Schematic view of the reactor system and the injection nozzles: (**a**) The producer gas partial oxidation system; (**b**) The primary air injection nozzles.

3.2. Introduction of the Combustion Equipment Grid Partitioning and Grid Independence Verification

The physical model of this study was constructed at a 1:1 scale based on the dimensions of the tar partial oxidation burner. A 3D model of the tar partial oxidation burner was developed, followed by meshing of the generated 3D model using ANSYS (Ansys 2020 R2) Meshing. The side view and cross-sectional view of the grid division are as shown in Figure 2. To accurately simulate chemical reactions during fluid flow, a refined mesh was applied to the region where combustion reactions occur, as shown in Figure 2.

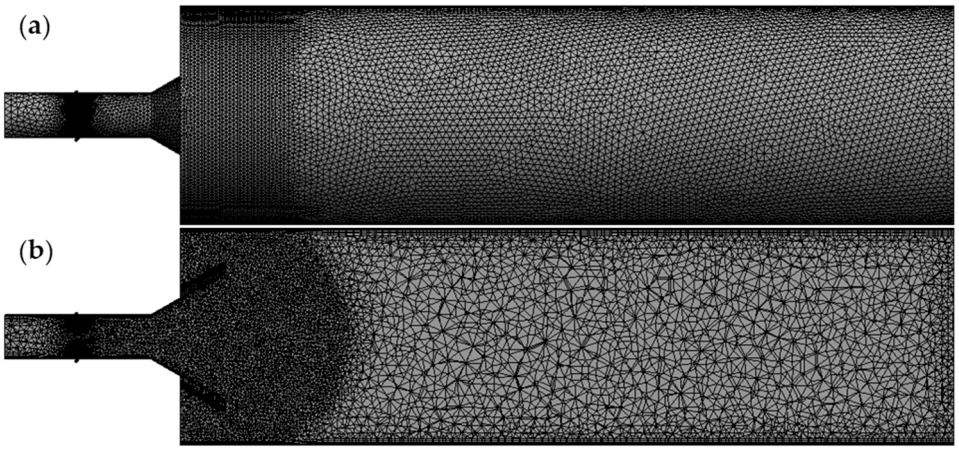


Figure 2. Meshing division: (**a**) side view; (**b**) sectional view.

A mesh independence verification was conducted to determine the optimal grid density for simulating the tar partial oxidation burner. The mesh was initially refined in the intense combustion and slow oxidation zones, resulting in a base grid of 2.13 million elements. The entire domain was then progressively refined, generating meshes ranging from 2.82 million to 3.96 million elements to evaluate the solution's independence from grid resolution.

To validate the accuracy of the computational mesh, a Grid Convergence Index (GCI) analysis was performed according to established methodologies [22–31]. The GCI is calculated using the following equation:

$$GCI = F_s \frac{|\varepsilon|}{r^p - 1} \tag{13}$$

where ε is the relative error between solutions on different grids, F_s is a safety factor. A value of 3 is used when comparing two grids, and 1.25 is used when comparing three or more grids. P is convergence accuracy, is specified as 1.97 in this context, and r is the grid refinement ratio.

The results of the GCI analysis are summarized in Table 1. The GCI values for meshes with 2.13, 2.82, and 3.31 million elements were calculated to be 0.34%, 0.43%, and 0.06%, respectively. All values fall below the 3% threshold, meeting the convergence criterion. This, coupled with an analysis of key field variables, confirms that the numerical solution is grid-independent beyond 3.31 million elements.

Table 1. Calculation of GCI.

Number of Grids (Million)	h_i (mm)	r	F(T) (K)	ε	GCI (%)
2.13	11.011	0.9666	733.56	0.00018	0.34
2.82	10.643	1.1310	733.69	0.00095	0.43
3.31	9.736	1.2710	734.39	0.00002	0.06
3.96	7.660		734.41		

3.3. Boundary Condition Setting

Prior to conducting numerical simulations in Fluent for the partial oxidation process in the reactor, boundary conditions were established per Table 2. The walls enforced a no-slip condition with zero species flux. The combustion domain featured a non-adiabatic flame zone, while boundaries were treated as adiabatic. The selection of boundary conditions was tailored to the specific characteristics of each reactor zone, with the determination of each parameter being based on empirical operational data.

Table 2. Partial oxidation burner wall boundary condition.

Wall Name	Boundary Setting
upper reactor wall	T = 773.15 K, ε = 0.6, thermal boundary
nozzle wall	T = 973.15 K, ε = 0.6, thermal boundary
lower burner wall	T = 473.15 K, ε = 0.6, thermal boundary

The reactor inlet boundary conditions are detailed in Table 3, while the outlet boundary corresponds to the product gas exit section at the top of the glass bell. The boundary conditions are configured as a pressure outlet, with the specified static pressure value set to 1 atm. The composition of the fuel mixture used in the experiment is shown in Table 4.

Table 3. Inlet parameter.

Items	Parameters	Units
Fuel inlet flow	40	L/min
Primary air inlet flow	8.0022~30.0008	L/min
Secondary air inlet flow	1~7	L/min
Tar inlet temperature	473.15	K
Nozzle inlet temperature	473.15	K
Reactor inlet temperature	473.15	K
Temperature of reactor wall	473.15	K
Turbulence model	Realizable k-ε model	

This experimental study is based on the tar composition from a downdraft gasifier. Specifically, because tertiary aromatics are predominant in the downdraft product spectrum,

naphthalene is used as a tar model compound to simulate raw producer gas. The specific fuel mixture composition is as shown in Table 4.

Table 4. Fuel mixture (mole%) composition.

Composition	CH_4 (%)	H_2 (%)	N_2 (%)	$C_{10}H_8$ (%)
Content	2	32	65.995	0.005

4. Results and Discussions

The primary air injector and secondary air injector are the two main types of oxygen introduced into the reactor. The primary air is used to form a stable and intense flame within the reactor, while the secondary air provides the oxygen required for the partial oxidation of tar. This part primarily examines the effects of these two oxygen introduction methods on the temperature distribution and tar conversion within the reactor.

4.1. Model Validation

The kinetic model was validated via CH_4 reforming experiments. Specifically, the CH_4 reforming experiments were conducted in a plug-flow reactor, with a temperature range from 1523 K to 1903 K and a reaction residence time of 2.1 s. The relevant experimental details are described in the reference [32]. Figure 3 shows a comparison between the experimental and simulation results for this process, and it can be seen that the kinetic simulation describes the process well. By observing the figure, it is evident that the simulation results for CO, H_2, CO_2, and CH_4 are largely consistent with the experimental results. However, due to the significant fluctuations in H_2O content in the experiments, there is some discrepancy between the simulation and experimental results, but the overall trends are consistent.

For the validation of the CFD-kinetic model, the simulation's boundary conditions align with the actual operating conditions, with simulated results compared to experimental measurements to validate the model's accuracy. Temperature data were measured at Z = 0.27 m section and compared with the simulated facet average temperature at corresponding section, demonstrating a strong alignment between the experimental and simulated results. As shown in Figure 4, the simulated results generally aligned with experimental results, with temperature error margins consistently remaining within 3%. which is consistent with findings in other studies where error margins are typically within 1–4.8% [29]. Although the simulation of total tar concentration did not perform as effectively as the temperature simulation, the results were still considered acceptable, as the model's validity was further supported by the consistent trends observed between simulated and experimental values within the validation range. This consistency underscores the reliability of the model in capturing key process behaviors.

The temperature profiles observed in Figure 4a indicate that as the primary air inlet flow increases from 0.20 to 0.75, both measured and simulated temperature exhibit a gradual upward trend, which aligns with the expected thermal behavior in gasification systems. However, when the secondary air inlet flow increases from 1 L/min to 7 L/min, the measured and simulated temperatures show a decreasing trend, as shown in Figure 4b, which contradicts the expected behavior. This discrepancy arises because the introduction of secondary air into the reaction system may react with flammable gases (e.g., H_2 and CH_4), promoting temperature elevation, yet the observed temperature decrease suggests a complex interplay between gas composition, flow dynamics, and thermal behavior. This inconsistency underscores the need for further analysis to clarify the underlying mechanisms.

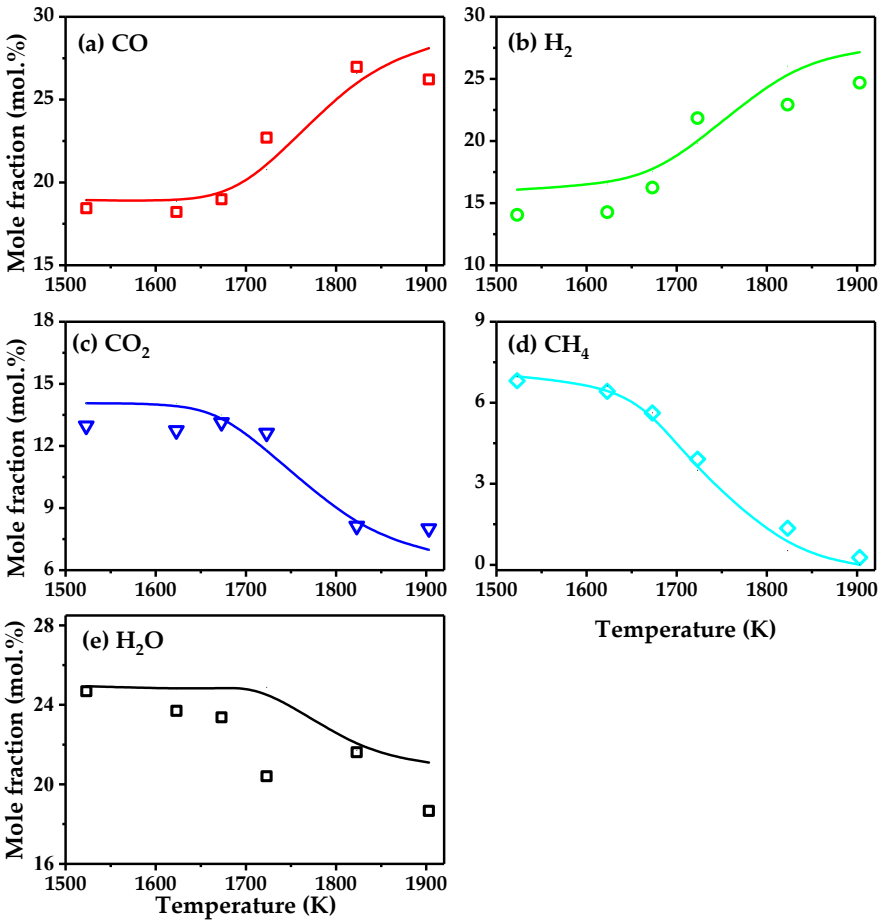


Figure 3. Validation of the kinetic model during the CH_4 conversion in a flow reactor: (**a**) CO; (**b**) H_2; (**c**) CO_2; (**d**) CH_4; (**e**) H_2O.

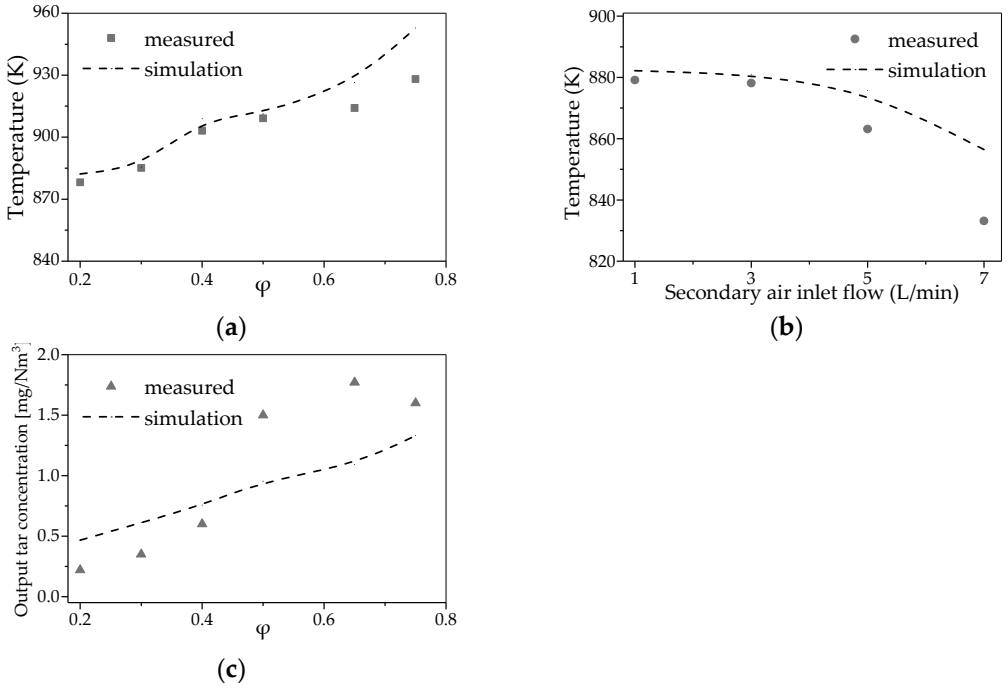


Figure 4. Model validation with variation air inlet: (**a**) Variation in temperature with primary air; (**b**) Variation in temperature with variation air inlet; (**c**) Variation in tar with primary air.

The simulated tar concentrations slightly differ from the experimental results, as shown in Figure 4c. The discrepancy between simulated and experimental total tar concentrations, may arise from simplifications in the measurement process. Specifically, the use of organic components such as benzene and naphthalene to represent specific tar fractions (e.g., one-ring and two-ring components) in measurements, as discussed in the work of Houben et al. [26], can introduce inherent errors. Additionally, the experimental measured tar content was relatively low, making accurate simulation of its concentration challenging. However, the experimental and simulated tar content trends are identical, indicating that the simulation of its behavior within the reactor remains reliable.

4.2. Influence of Air Inlet on Temperature Distribution and Tar Reduction in a Partial Oxidation Reactor

4.2.1. Influence of Primary Air Inlet on the Temperature Field Within the Reactor

The likelihood of obtaining more accurate simulation results by adjusting model parameters or employing finer grids is possible, as adjusting parameters can enhance prediction accuracy and finer grids can lead to more accurate simulations. However, this is not the focus of our study. We assume that the current computational setup is sufficient to represent the combustion behavior within the reactor for comparing different φ conditions, although it may not fully align with experimental data. The computations for the burner are performed using only the k-ε model with the kinetic model. We assume that the results obtained under different φ conditions maintain the same level of accuracy, and thus using them for comparative analysis is credible.

The flame and burner advance along the *Z*-axis in the reactor modeling process. Simulation studies revealed that the combustion reactions of primary air primarily mainly occur in the region from Z = 0.05 m to Z = 0.09 m cross-sections. Therefore, the temperature distribution and component distribution were primarily investigated in the region from Z = 0.06 m to Z = 0.09 m cross-sections. Figure 5 demonstrates the temperature distribution in the region from Z = 0.05 m to Z = 0.09 m cross-sections for primary air φ values of 0.20, 0.40, and 0.75. It can be observed that the solutions obtained for different φ values exhibit significantly different behaviors. Primary air injected through the primary air injection nozzles (as shown in Figure 1) mixes with the tar within the reactor and subsequently undergoes combustion. In effect, the central lower portion of the burner remains largely "cold" with the flame primarily occurring near the walls. It is noteworthy that such configurations should be avoided, as they are likely to lead to overheating and rapid degradation of the burner walls.

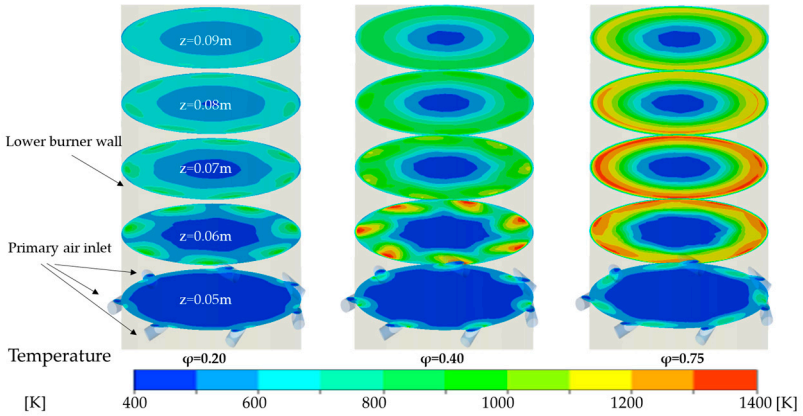
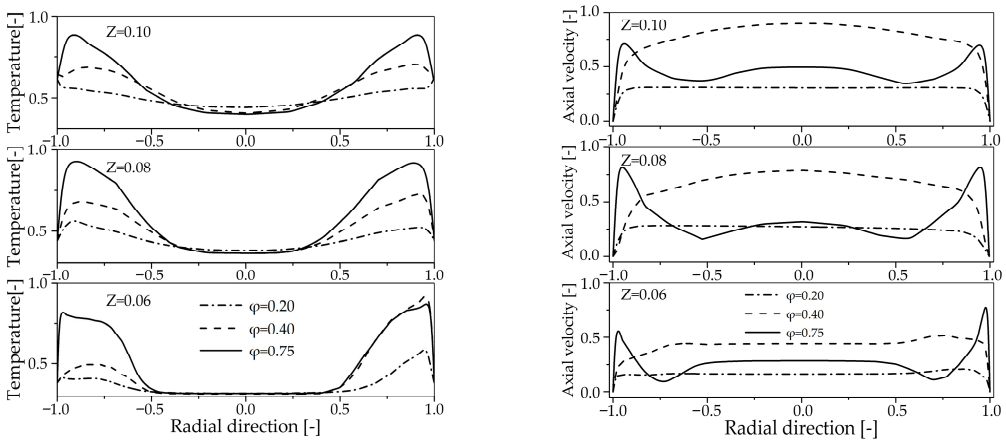


Figure 5. Temperature distribution in the radial cross-section planes at different φ.

The primary air can enhance the maximum temperature of the flame and shift the combustion zone further downstream. The comparison of different φ demonstrates that the

primary air inlet flow rate considerably affects the combustion state of the tar, as reflected in the temperature distributions across various cross-sections in Figure 5. To further illustrate the effect of φ on the temperature distribution inside the reactor, Figure 5 shows the radial profiles of temperature and axial velocity at z = 0.60 m, 0.80 m, and 0.10 m for different φ. At φ = 0.20, combustion occurs mainly between Z = 0.05 m and 0.06 m. The temperature gradient at the Z = 0.06 m cross-section is relatively small, with a maximum temperature of 892.17 K (Figure 6a), indicating less intense combustion. When φ is increased to 0.40, the combustion zone shifts to the Z = 0.06 m cross-section, where a larger temperature gradient is observed and the maximum temperature rises significantly to 1379.47 K. Simultaneously, the maximum temperature at Z = 0.07 m increases to 1077.39 K. As φ is further raised, the combustion region continues to move downstream. At φ = 0.75, the main combustion zone approaches Z = 0.07 m, with maximum temperatures of 1308.75 K and 1321.02 K at the Z = 0.06 m and Z = 0.07 m cross-sections, respectively. At this point the peak temperature is located at the Z = 0.067 m cross-section, measuring 1398.63 K. These results indicate that higher φ values not only intensify combustion but also shift the combustion zone further downstream within the reactor.



(**a**) (**b**)

Figure 6. Radial profiles of the temperature and axial velocity at z = 0.60 m, 0.80 m, 0.10 m for the different primary air injection: (**a**) Temperature; (**b**) Axial velocity.

As the primary air flow increases, the temperature near the reactor wall increases, as shown in Figure 6a. The primary air is injected into the reactor at a 45 angle from the central axis, which means the injected fluid possesses a strong radial velocity component. This configuration enhances the radial momentum of the flow, leading to increased combustion intensity near the reactor walls as the primary air flow increases. This results in elevated temperatures near the wall region with higher primary air flow, as clearly observed in the Z = 0.08 m cross-section (Figure 6a). This trend, however, is less evident in the Z = 0.06 m and Z = 0.10 m cross-sections. At Z = 0.06 m, combustion is in its initial stages, leading to uneven heat transfer and temperature distribution. At Z = 0.10 m, sufficient heat transfer has occurred: for low φ values, temperatures are more uniform and relatively low, whereas for high φ values, both temperatures and thermal gradients remain significantly higher.

With the increase in primary air flow, the radial temperature gradient within the reactor gradually increases, which can be attributed to the gradually enhanced swirling phenomenon. To investigate this, 3D simulations were employed to plot velocity vectors at different cross-sections downstream of the combustor inlet, as shown in Figure 7. Additionally, the normalized axial velocity at different cross-sections is shown in Figure 6b. From Figure 7, it is observed that a strong swirl flow is present near the reactor walls, accompanied by a significant axial velocity, as shown in Figure 6b. As the position moves

from the reactor wall toward the center, both the tangential and axial velocity components gradually decrease, with the tangential velocity reaching zero and the axial velocity reducing significantly at the reactor center. As the primary air flow increases, the radial velocity component of the fresh air entering the reactor increases. This leads to higher temperatures in the combustion zone, which in turn causes the high-temperature materials to accumulate near the reactor walls. Consequently, the radial temperature gradient within the reactor increases.

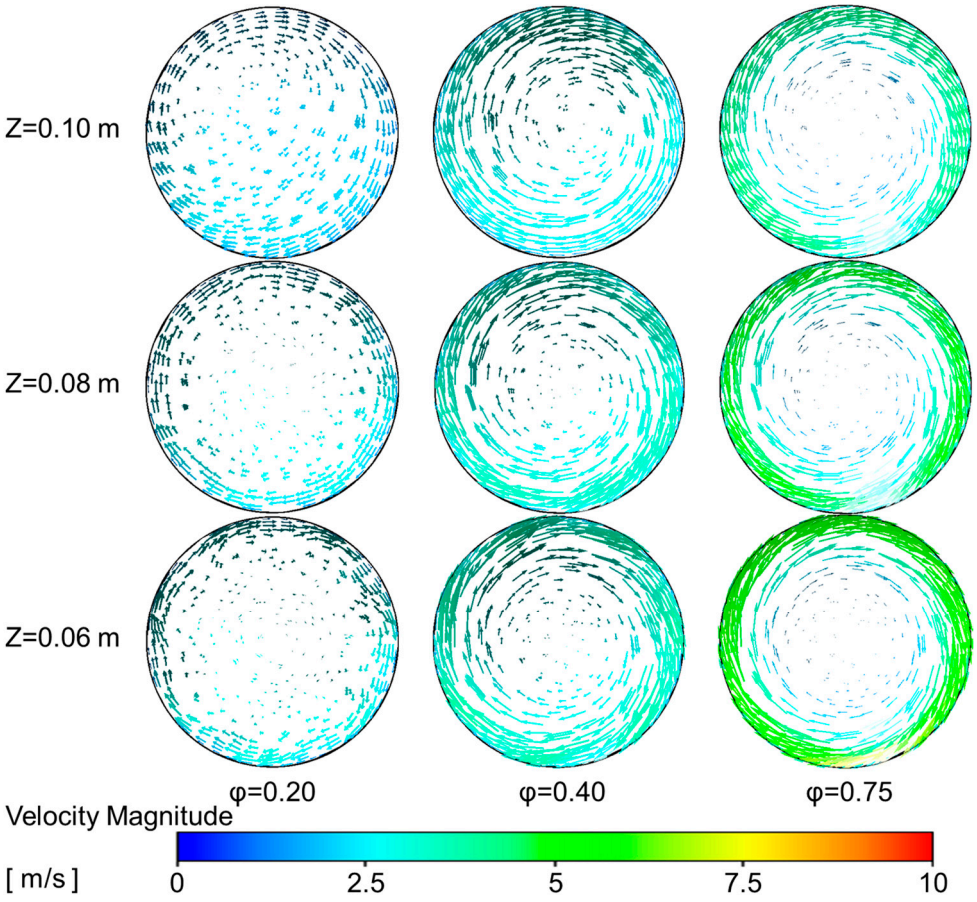


Figure 7. Velocity vectors plot at different radial cross-section downstream the combustor inlet.

4.2.2. Influence of Primary Air Inlet on the Chemical Reaction Dynamics Within in the Reactor

Although the above analysis provides detailed insights into the flame/flow interaction within the combustion chamber, the chemical reactions occurring within the chamber and the distribution of key component concentrations are equally important from the perspective of tar conversion. The mole fractions of species along the radial direction at three axial distances are shown in Figure 8. The values of species fractions are normalized by the results obtained from the simulation. Specifically, in Figure 8, $C_{10}H_8$ and CH_4 are reactants, while soot and C_6H_6 are intermediate products formed during the reaction, which gradually disappear as the flame develops. Therefore, the distribution of these components is only shown between Z = 0.06 and Z = 0.08 m in Figure 8.

The reactant $C_{10}H_8$ and CH_4 primarily undergo significant conversion in the high-temperature zone of the reactor. This observation is supported by comparing the mole fractions of $C_{10}H_8$ and CH_4 (Figure 8a,b) and the corresponding temperature profile (Figure 6a). For example, at Z = 0.06 m and Z = 0.08 m cross-sections, the mole fraction of $C_{10}H_8$ decreases to nearly zero in high-temperature zones, while it remains at a high

level in the low-temperature regions near the reactor center. However, at Z = 0.10 m, this pattern is not as pronounced, primarily due to the distance from the primary air injection nozzles, which allows for thorough mixing of the reaction mixture, leading to a decrease in $C_{10}H_8$ mole fraction with increasing primary air flow.

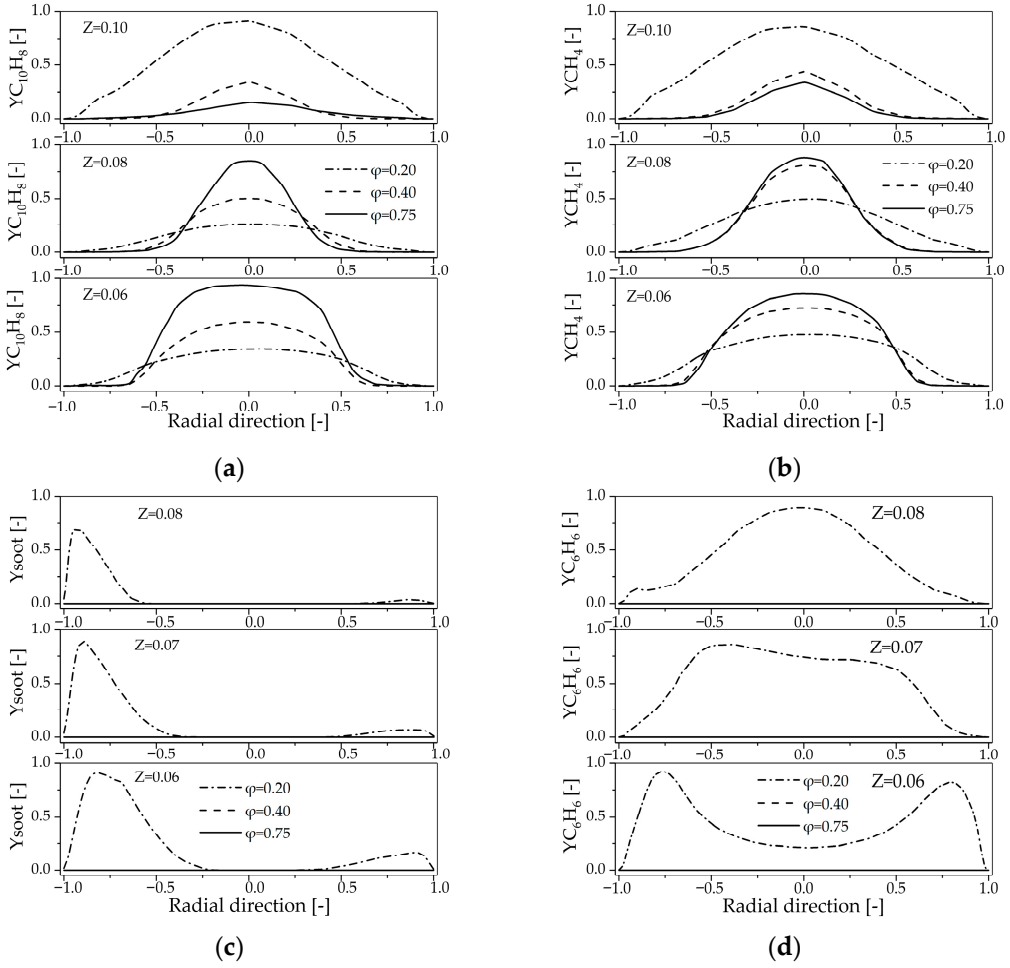


Figure 8. Radial profiles of the species mole fraction at z = 0.06 m, 0.08 m, 0.10 m for the different primary air inlet: (**a**) $C_{10}H_8$; (**b**) CH_4; (**c**) Soot; (**d**) C_6H_6.

The conversion of reactants $C_{10}H_8$ and CH_4 primarily occurs within the combustion region between Z = 0.06 m and Z = 0.07 m along the axial direction. The normalized maximum mole fractions of $C_{10}H_8$ are 9.33×10^{-6} at Z = 0.06 m, 8.13×10^{-7} at Z = 0.08 m, and 7.27×10^{-8} at Z = 0.10 m, showing a clear trend of decreasing concentration with increasing height. This indicates that the conversion of $C_{10}H_8$ predominantly occurs between Z = 0.06 m and Z = 0.07 m, where the conversion rate of $C_{10}H_8$ is over 90%. This observation aligns with the enhanced reaction kinetics at elevated temperatures, as supported by the principle that temperature increases reaction rates. The data highlight the spatial dependence of reaction dynamics, emphasizing the importance of temperature gradients in chemical conversion processes.

Soot and C_6H_6 are important intermediate species formed during the combustion process, and their production is significantly inhibited by primary air flow. Although their maximum mole fraction in the reactor—on the order of 1×10^{-11}—are negligible compared to reactants like CH_4, their distribution within the reactor reflects the combustion conditions of reactants. Therefore, studying their mole fraction profile is crucial for optimizing reactor design. As shown in Figure 8c,d, their formation is strongly influenced by the φ. For example, the maximum mole fraction of soot decreases markedly with increasing φ: from

1.03×10^{-11} at φ = 0.20 to 4.20×10^{-19} at φ = 0.40 and 4.24×10^{-21} at φ = 0.75 in the Z = 0.08 m cross-section. Further analysis of the O_2 concentration reveals that, likely due to the presence of a large amount of H_2 in the reactor, the O_2 in the reactor is rapidly consumed near the primary air inlet nozzles, resulting in its concentration being much lower than that of soot after the Z = 0.06 cross-section. Therefore, the influence of O_2 concentration on the variation in soot content can be considered negligible. This indicates that increasing primary air flow reduces the formation of intermediate products like soot and C_6H_6 during the reaction, but this reduction is not due to direct contact with O_2.

The formation of soot is more complex than that of C_6H_6, resulting in less regular mole fraction profiles for soot compared to C_6H_6, as shown in Figure 8c,d. Research indicates that soot is formed through the polymerization of $C_{10}H_8$, while C_6H_6 primarily originates from the decomposition of $C_{10}H_8$ [22]. The region where C_6H_6 is produced coincides with the region where $C_{10}H_8$ is consumed, as shown in Figure 8. By comparing Figure 6a, it can be observed that as φ increases from 0.20 to 0.75, the temperature at the Z = 0.08 m cross-section rises from 880.71 K to 1321.07 K, and the maximum temperature inside the reactor also gradually increases. This phenomenon may primarily stem from the influence of and temperature, as soot formation is highly dependent on this parameter [33].

4.3. Influence of Secondary Air Inlet on Temperature Distribution and Tar Reduction in a Partial Oxidation Reactor

The experimental findings by Houben et al. [26] highlight a notable divergence between the intended and actual effects of secondary air injection in the reactor. While secondary air is introduced as a co-flow to regulate back pressure and is designed to participate in partial oxidation, its increase leads to an unexpected decrease in temperature—contrary to the conventional expectation that additional oxygen should enhance oxidation and raise temperatures in a reducing atmosphere. This section will elaborate on the effects of secondary air flow on the partial oxidation burner, in terms of temperature distribution and component distribution, among other aspect.

4.3.1. Subsubsection Influence of Secondary Air Inlet on the Temperature Field Within the Reactor

Figure 9 illustrates the horizontal cross-sectional temperature distribution within the burner for secondary air inlet flow rates of 1 L/min, 5 L/min, and 7 L/min, observed at axial positions ranging from Z = 0.13 m to Z = 0.27 m. The Z = 0.13 m plane represents the secondary air injection plane, where the secondary air is introduced into the combustion system, while the Z = 0.27 m plane corresponds to the temperature measurement plane, where temperature distributions are recorded. These cross-sectional planes are critical for analyzing the combustion, as they provide insights into the spatial distribution of temperature and the influence of secondary air on the tar conversion.

Increasing secondary air flow reduces the measured temperature, mainly because it expands the range of low-temperature regions in the reactor's center, leading to a lower measured temperature. As illustrated in Figure 9, the temperature distributions across different flow rates exhibit a similar central low-temperature region. However, as the secondary air flow rate increases, the area of this low-temperature region expands noticeably at the measurement plane (Z = 0.27 m). This expansion aligns with the experimentally observed decrease in temperature, suggesting that higher secondary air flow enhances cooling region. A possible reason is that the introduction of secondary air as a co-flow alters the internal flow dynamics of the reactor.

Figure 10 shows the radial profiles of the temperature and axial velocity at different axial positions. It can be observed that the axial velocity is significantly higher in the central low-temperature region of the reactor. As illustrated in Figure 10a, at a secondary air flow

of 7 L/min, the temperature at the Z = 0.17 m cross-section is lower in the reactor center, where the axial velocity is also highest. The likely reason is that increased secondary air flow introduces cooler fresh air, which, when mixing with primary air and hot materials, reduces the temperature in the reactor center. Experimental temperature measurements are taken at the Z = 0.27 m cross-section, where secondary air addition reduces temperature while increasing axial velocity, leading to observed temperature decreases with increasing secondary air flow.

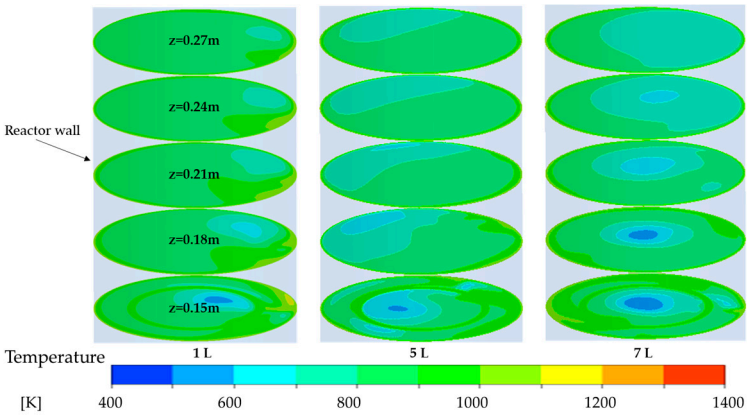


Figure 9. Temperature distribution in the radial cross-section planes at different secondary air flow rate.

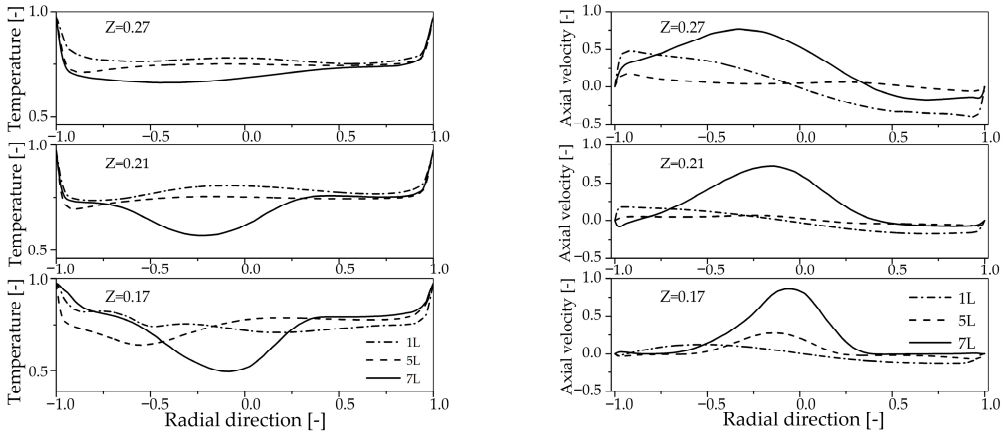


Figure 10. Radial profiles of the temperature and axial velocity at z = 0.17 m, 0.21 m, 0.27 m for the different secondary air injection: (**a**) Temperature; (**b**) Axial velocity.

Figure 11 shows the changes in measured temperature and output temperature as the secondary air flow rate increases. The data shown that introducing secondary air reduces the measured temperature while simultaneously increasing the output temperature. Specifically, when the secondary air flow is 1 L/min, the measured and output temperatures are nearly identical. However, as the secondary air flow increases, the discrepancy between the two temperatures gradually widens. When the secondary air flow increases from 1 L/min to 7 L/min, the measured temperature decreases from 879.15 K to 833.15 K; however, the output temperature exhibits a rising trend. This indicates that the difference between the measured and output temperatures is primarily influenced by the secondary air flow. The primary reason for this discrepancy is that the dilution effect of cold secondary air reduces the measured temperature, while the increased secondary air flow enhances the oxidation reaction, thereby promoting an increase in the outlet temperature.

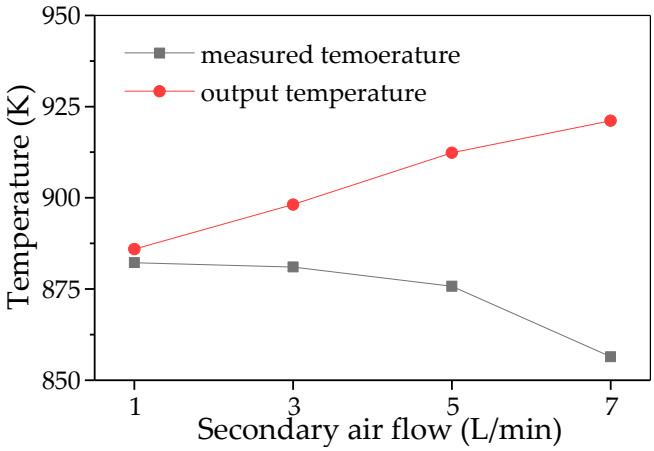


Figure 11. The temperature comparison of measured point and output.

The increase in secondary air flow enhances the flow dynamics within the reactor. To analyze the flow characteristics, Figure 11 illustrate the velocity magnitude at different cross-sections. Observations indicate that varying secondary air flow leads to irregular flow patterns. Specifically, Figure 10b shows that increasing secondary air inlet flow gradually increases the axial velocity at the reactor center. As shown in Figure 12, at a secondary air flow of 1 L/min, the reactor exhibits a strong swirl flow. However, as the secondary air flow increases, the axial velocity at the reactor center gradually increases, while the swirl flow within the reactor diminishes. This indicates that secondary air enhances the axial velocity at the reactor center while reducing the swirl flow within the reactor.

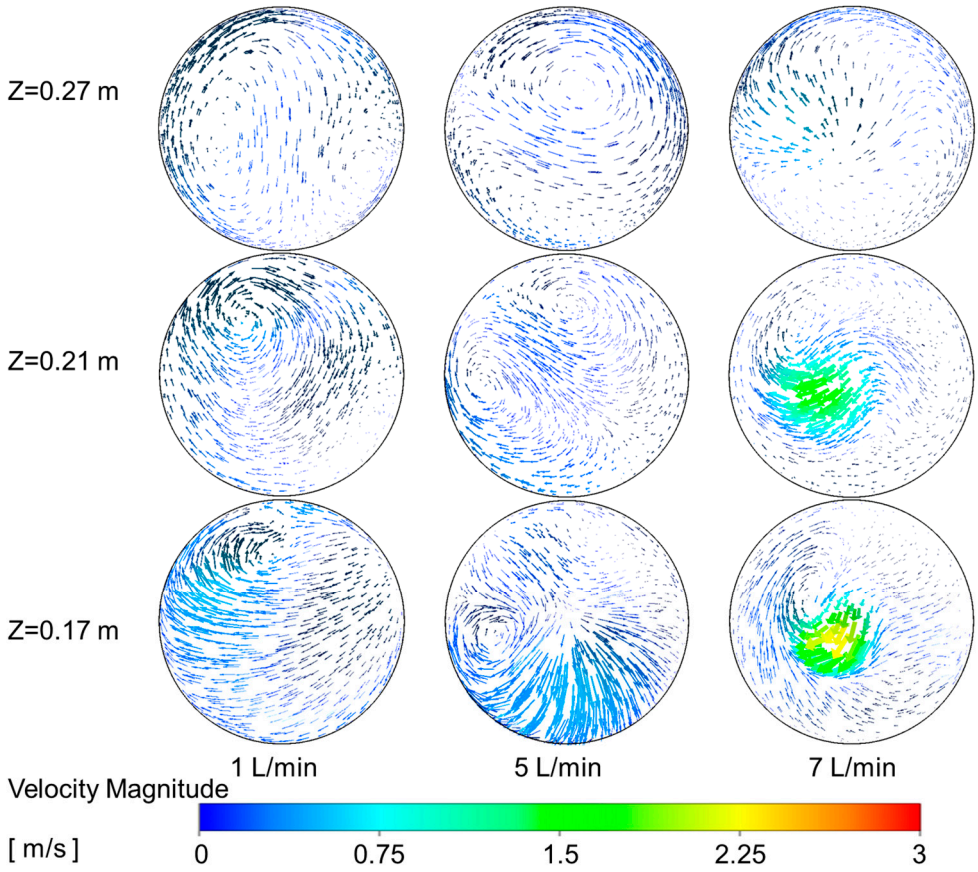


Figure 12. Velocity vectors plot at different radial cross-section downstream the secondary air inlet.

To better investigate the influence of secondary air on the flow field inside the reactor, Figure 13 shows the variation in turbulence intensity inside the reactor with increasing secondary air flow rate. From the figure, it can be observed that the distribution of turbulence intensity inside the burner can be mainly divided into two parts: the straight section and the diffusion section. Among these, the turbulence in the straight section is primarily influenced by the primary air flow, whereas the turbulence intensity in the diffusion section is mainly affected by the secondary air flow. As the primary air flow rate increases from 1 L/min to 7 L/min, the turbulence intensity in the diffusion section of the burner rises from 0.50 to 1.0. The main reason is likely that the secondary air primarily contacts the fuel in the diffusion section, resulting in the phenomenon where increasing the secondary air flow rate leads to an enhancement of turbulence intensity in the diffusion section of the burner.

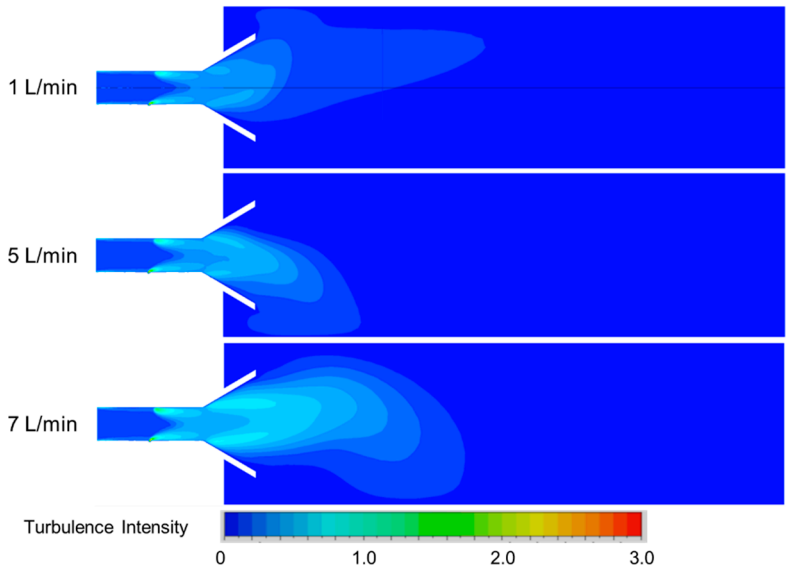


Figure 13. Turbulence intensity in the axial cross-sectional planes at different secondary air flow.

4.3.2. Influence of Secondary Air Inlet on the Chemical Reaction Dynamics Within the Reactor

Figure 14 shows the radially distributed mole fractions of key species at axial positions Z = 0.17 m, 0.21 m, and 0.27 m, normalized using simulation results. As in Figure 8, $C_{10}H_8$ and CH_4 are tracked as reactants, while soot and C_6H_6 are examined as representative intermediate products. Their spatial distributions provide insight into reaction progress and species conversion under varying flow and temperature conditions.

The increase in secondary air inlet flow generally enhances the conversion of $C_{10}H_8$ and CH_4. As shown in Figure 14a,b, although the mole fraction profiles of $C_{10}H_8$ and CH_4 at Z = 0.17 m, 0.21 m, and 0.27 m are irregular, the overall concentration of these species decreases with increasing secondary air flow in the reactor. As shown in Figure 12, the velocity distribution at these cross-sections is uneven, which may be the primary reason for the irregularity in the mole fraction profiles.

The influence of secondary air on the conversion of reactants such as $C_{10}H_8$ and CH_4 is limited. Specifically, at a secondary air flow of 1 L/min, 5 L/min, and 7 L/min, the maximum mole fractions of $C_{10}H_8$ are 2.75×10^{-8}, 1.28×10^{-8}, and 1.29×10^{-9}, respectively. These values remain close to the baseline mole fraction of 7.27×10^{-8} (the mole fraction in burner before secondary air reaction), indicating that while secondary air promotes some conversion, its overall effect on $C_{10}H_8$ consumption is limited. A similar trend is observed for CH_4, suggesting that the influence of secondary air on reactant conversion is generally limited.

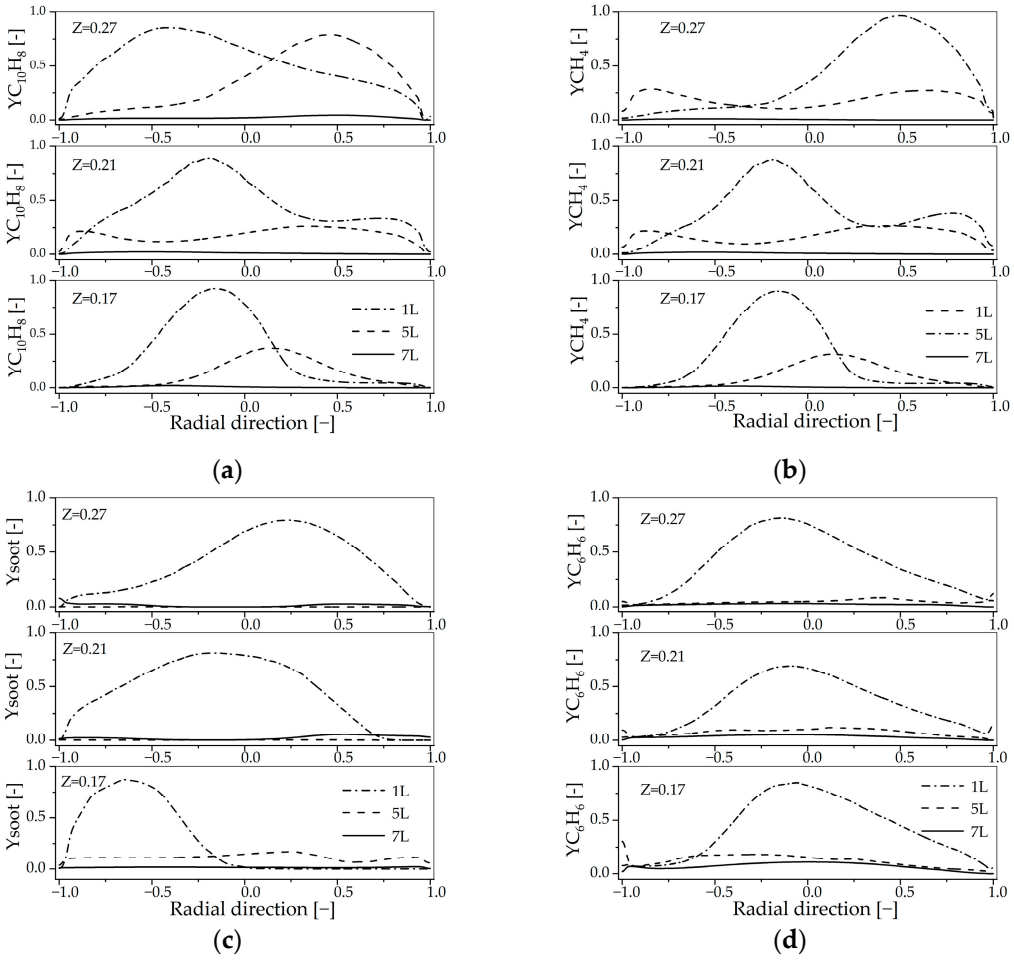


Figure 14. Radial profiles of the species mole fraction at z = 0.17 m, 0.21 m, 0.27 m for the different secondary air inlet: (**a**) $C_{10}H_8$; (**b**) CH_4; (**c**) Soot; (**d**) C_6H_6.

The inhibitory effect of secondary air on intermediate products such as soot and C_6H_6 is limited. As shown in Figure 14c, the yields of both species decrease with increasing secondary air flow. For example, the maximum soot mole fractions at Z = 0.27 m are 2.62×10^{-10}, 5.11×10^{-11}, and 6.52×10^{-12} at secondary air flows of 1 L/min, 5 L/min, and 7 L/min, respectively. Upon investigation, the current O_2 concentration is 1.25 or lower, so the direct inhibitory effect of O_2 on soot is negligible at this point, as analyzed in the previous section, a decrease in temperature may favor soot formation; however, secondary air has a certain diluting effect on the fuel material, thereby reducing soot content. So, the changes in soot and other intermediate products may result from dual effects of temperature and dilution.

Table 5 illustrates the effects of different O_2 injection methods on peak flame temperature, tar conversion efficiency, and soot yield. For comparison, the evaluation parameters for primary and secondary air inputs were calculated with the initial plane set as the fuel inlet plane and the output planes at Z = 0.09 m and Z = 0.27 m, respectively. Analysis shows that primary air combustion converts most of the tar and significantly suppresses soot formation. Specifically, after primary air combustion, tar conversion efficiency and soot yield are 99.13% and 0.0504%, respectively; based on the primary air combustion, after secondary air combustion, the tar conversion efficiency increases to 99.98% and the soot yield decreases to 0.0460%, respectively. This is likely due to the higher combustion peak temperature with primary air input (1398.63 K) compared to secondary air input (1279.17 K), as presented in Table 4.

Table 5. Comparison of parameters for different O_2 injection methods.

O_2 Injection Methods	T_{max} (K)	η_{tar} (%)	Y_{soot} (%)
Primary air input	1398.63	99.13	0.0504
Secondary air input	1279.17	99.98	0.0460

The use of primary air injection for oxygen introduction into the reactor is a reasonable approach, as it facilitates more stable flame control and enhanced combustion efficiency. Compared to secondary air injection, primary air injection allows for better control of burner reactions. Specifically, increasing primary air flow enhances flame stability, raises flame temperature, and improves tar conversion. In contrast, secondary air injection tends to lead to irregular flow patterns and reduced reaction stability, as well as limited effects on reactant conversion and intermediate product inhibition. These findings align with studies indicating that direct oxygen injection (e.g., primary air injection) can improve combustion stability and reaction efficiency.

5. Conclusions

This study developed a comprehensive computational model to investigate the tar conversion process in a partial oxidation burner, with a specific focus on the effects of different oxygen injection methods. The primary research question examined how variations in primary air flow and secondary air flow influence temperature distribution, flame stability, and the conversion of key organic components such as $C_{10}H_8$ and CH_4. The findings are summarized as follows:

The newly developed model for tar conversion has been successfully validated using partial oxidation experimental data. The novelty of this model lies in its application of the Arrhenius equation to describe soot nucleation and surface growth processes, thereby comprehensively integrating the mechanisms of soot formation, tar reaction, and small molecule combustion during the tar conversion process. Compared with experimental results, the simulation temperature error remains within 3%. At the same time, the model could well predict tar content trends.

The simulation results indicate that an increase in primary air flow elevates the peak flame temperature and shifts the combustion zone further downstream. Raising φ from 0.20 to 0.75 causes the peak flame temperature to rise from 892.17 K to 1398.63 K and shifts the flame combustion zone from Z = 0.06 m to Z = 0.07 m. Increasing the primary air flow could enhance the conversion of $C_{10}H_8$ and CH_4, which primarily occurs within the combustion region, where their conversion exceeds 90%. Rasing φ from 0.20 to 0.75 could reduce the maximum $C_{10}H_8$ mole fraction from 4.20×10^{-11} to 4.24×10^{-21}. Secondary air inlet has a weaker effect on tar conversion compared to primary air inlet. When secondary air flow increases from 1 L/min to 7 L/min, unexpected cooling occurs near the centerline, reducing measured temperatures from 879.15 K to 833.15 K, even as outlet temperatures increase. The influence of secondary air on reactant conversion is limited, with the conversion rate being only about 1% at this point. Rasing secondary air flow from 1 L/min to 7 L/min only reduces the maximum soot mole fraction from 2.62×10^{-10} to 6.52×10^{-12}, which, compared to primary air flow, has a relatively limited effect. The coupled flow-reaction simulation results demonstrate that primary air flow significantly enhances flame stability, increases flame temperature, and improves tar conversion. In contrast, secondary air flow does not form a stable and sustained flame and does not substantially promote tar conversion. Consequently, the use of primary air injection for oxygen introduction into the reactor is a reasonable approach, as it results in a more stable flame and more efficient tar conversion.

Through the simulation and verification in this work, this model can be widely applied to the simulation study of biomass raw producer gas partial oxidation reactor. The model will next be applied to the simulation and analysis of biomass pretreatment and gasification processes. For this purpose, the model needs to introduce different variables to enhance its application capability in complex biomass pre-treatment and gasification systems.

Author Contributions: Conceptualization, Y.W. and G.C.; methodology, Y.W.; software, S.W.; formal analysis, Y.W., S.W., D.H. and Z.B.; validation, S.W., D.H., Z.B. and C.L.; resources, C.L.; data curation, Y.W.; writing—original draft preparation, Y.W.; writing—review and editing, G.C., J.Z. and Y.F.; visualization, G.C.; supervision, Y.F.; project administration, J.Z. and Y.F.; funding acquisition, C.L. All authors have read and agreed to the published version of the manuscript.

Funding: This research was funded by the Strategic Priority Research Program of the Chinese Academy of Sciences, grant number XDA29050600.

Data Availability Statement: The original contributions presented in this study are included in the article. Further inquiries can be directed to the corresponding author.

Conflicts of Interest: The authors declare no conflict of interest.

References

1. Nikolina, S. International Renewable Energy Agency (IRENA). 2024. Available online: https://www.irena.org/Energy-Transition/Outlook (accessed on 12 May 2025).
2. Sher, F.; Hameed, S.; Omerbegović, N.S.; Chupin, A.; Hai, I.U.; Wang, B.; Teoh, Y.H.; Yildiz, M.J. Cutting-edge biomass gasification technologies for renewable energy generation and achieving net zero emissions. *Energy Convers. Manag.* **2025**, *323*, 119213. [CrossRef]
3. Reina-Guzmán, S.; Ayabaca-Sarria, C.; Tipanluisa-Sarchi, L.; Venegas-Vásconez, D. Thermochemical Conversion of Biomass: Aspen Plus® Modeling of Sugarcane Bagasse Gasification for Syngas Integration. *Processes* **2025**, *13*, 3037. [CrossRef]
4. Wang, B.F.; Wang, L.; Sadeq, A.M.; Alsenani, T.R.; Muhammad, T. Biomass gasification combined with a novel heat integration design for sustainable energy supply programs: Comprehensive thermodynamic, environmental, and economic evaluations. *Energy* **2025**, *337*, 138560. [CrossRef]
5. Paramasivam, P.; Alruqi, M.; Ağbulut, Ü. Experimental simulation and analysis of Acacia Nilotica biomass gasification with XGBoost and SHapley Additive Explanations to determine the importance of key features. *Energy* **2025**, *327*, 136291. [CrossRef]
6. Shen, Y. Biomass pretreatment for steam gasification toward H2-rich syngas production–An overview. *Int. J. Hydrog. Energy* **2024**, *66*, 90–102. [CrossRef]
7. Zou, L.; Guo, S.; Feng, Z.; Shao, H.; He, X.; Wu, A. The effects of conventional and microwave torrefaction on waste distiller's grains and its steam gasification characteristics. *Fuel* **2025**, *380*, 133163. [CrossRef]
8. Ge, S.; Tahir, M.H.; Chen, D.; Hong, L.; Feng, Y.; Huang, Z. MSW pyro-gasification using high-temperature CO_2 as gasifying agent: Influence of contact mode between CO_2, char and volatiles on final products. *Waste Manag.* **2023**, *170*, 112–121. [CrossRef]
9. Saleem, F.; Raashid, M.; Rehman, A.; Khoja, A.H.; Abbas, A.; Gul, S. Dielectric barrier discharge reactor application in biomass gasification tar removal. *Renew. Sustain. Energy Rev.* **2025**, *208*, 114963. [CrossRef]
10. Díez, D.; Urueña, A.; Antolín, G. Investigation of Ni–Fe–Cu-Layered Double Hydroxide Catalysts in Steam Reforming of Toluene as a Model Compound of Biomass Tar. *Processes* **2021**, *9*, 76. [CrossRef]
11. Chang, T.; Zhang, T.; Wang, Y.; Labidi, A.; Leus, K.; De Geyter, N. Plasma-catalytic reforming of toluene over Ni/HZSM-5 catalysts: Synergistic effect and reaction mechanism. *Chem. Eng. J.* **2025**, *520*, 166113. [CrossRef]
12. Talero, G.; Kansha, Y. Atom economy or product yield to determine optimal gasification conditions in biomass-to-olefins biorefinery. *Chem. Eng. Res. Des.* **2023**, *199*, 689–699. [CrossRef]
13. Wang, Y.; Zhang, J.; Liang, W.; Cao, G.; Li, C.; Zhao, J.; Fang, Y. Kinetic Analysis of Biomass Gasification Coupled with Non-Catalytic Reforming to Syngas Production. *J. Fuel Chem. Technol.* **2023**, *51*, 921–929. [CrossRef]
14. Errekatxo, A.; Ibarra, A.; Gutierrez, A.; Bilbao, J.; Arandes, J.M.; Castaño, P. Catalytic deactivation pathways during the cracking of glycerol and glycerol/VGO blends under FCC unit conditions. *Chem. Eng. J.* **2017**, *307*, 955–965. [CrossRef]
15. Anis, S.; Zainal, Z.A. Tar reduction in biomass producer gas via mechanical, catalytic and thermal methods: A review. *Renew. Sust. Energy Rev.* **2011**, *15*, 2355–2377. [CrossRef]
16. Tian, Y.; Du, J.; Luo, Z.; He, D.; Ma, W.; Zhou, X.; Liang, S.; Yuan, L. Kinetic study on biomass gasification coupled with tar reforming for syngas production. *Biomass Conv. Bioref.* **2023**, *14*, 28377–28385. [CrossRef]

17. Su, Y.; Luo, Y.; Chen, Y.; Wu, W.; Zhang, Y. Experimental and numerical investigation of tar destruction under partial oxidation environment. *Fuel Process. Technol.* **2011**, *92*, 1513–1524. [CrossRef]
18. Demol, R.; Ruiz, M.; Schnitzer, A.; Herbinet, O.; Mauviel, G. Experimental and modeling investigation of partial oxidation of gasification tars. *Fuel* **2023**, *351*, 128990. [CrossRef]
19. Hoeven, T. Partial Product Gas Combustion for Tar Reduction. Ph.D. Thesis, Eindhoven University of Technology, Eindhoven, The Netherlands, 2007.
20. Wu, W.G.; Luo, Y.H.; Chen, Y.; Su, Y.; Zhang, Y.L.; Zhao, S.H.; Wang, Y. Experimental investigation of tar conversion under inert and partial oxidation conditions in a continuous reactor. *Energy Fuel* **2011**, *25*, 2721–2729. [CrossRef]
21. Houben, M.; De Lange, H.; Van Steenhoven, A. Tar reduction through partial combustion of fuel gas. *Fuel* **2005**, *84*, 817–824. [CrossRef]
22. Jess, A. Mechanisms and kinetics of thermal reactions of aromatic hydrocarbons from pyrolysis of solid fuels. *Fuel* **1996**, *75*, 1441–1448. [CrossRef]
23. Svensson, H.; Tunå, P.; Hulteberg, C.; Brandin, J. Modeling of soot formation during partial oxidation of producer gas. *Fuel* **2013**, *106*, 271–278. [CrossRef]
24. Wongchang, T.; Patumsawad, S.; Fungtammasan, B. An analysis of wood pyrolysis tar from high temperature thermal cracking process. *Energy Sources Part A Recovery Util. Environ. Eff.* **2013**, *35*, 926–935. [CrossRef]
25. Zhang, R.; Zhao, S.; Luo, Y. Experimental and modeling investigation on the effect of intrinsic and extrinsic oxygen on biomass tar decomposition. *Energy Fuels* **2017**, *31*, 8665–8673. [CrossRef]
26. Houben, M.P. Analysis of Tar Removal in a Partial Oxidation Burner. Ph.D. Thesis, Eindhoven University of Technology, Eindhoven, The Netherlands, 2004. [CrossRef]
27. Williams, F.A. *Combustion Theory*; CRC Press: Boca Raton, FL, USA, 2018.
28. Putra, B.A.; Ertesvåg, I.S. Eddy Dissipation Concept (EDC) with Batch Reactor Fine Structures Model for Flames Toward Low Turbulence. *Combust. Sci. Technol.* **2025**, 1–27. [CrossRef]
29. Zheng, J.; Du, M.; Xiao, Z.; Zhu, X. Simulation of Soot Formation in Pulverized Coal Combustion under O_2/N_2 and O_2/CO_2 Atmospheres. *ACS Omega* **2024**, *9*, 22051–22064. [CrossRef] [PubMed]
30. Freitas, C.J. The issue of numerical uncertainty. *Appl. Math. Model.* **2002**, *26*, 237–248. [CrossRef]
31. Manna, P.; Dharavath, M.; Sinha, P.; Chakraborty, D. Optimization of a flight-worthy scramjet combustor through CFD. *Aerosp. Sci. Technol.* **2013**, *27*, 138–146. [CrossRef]
32. Valin, S.; Cances, J.; Castelli, P.; Thiery, S.; Dufour, A.; Boissonnet, G.; Spindler, B. Upgrading biomass pyrolysis gas by conversion of methane at high temperature: Experiments and modelling. *Fuel* **2009**, *88*, 834–842. [CrossRef]
33. Naseri, A.; Kholghy, M.R.; Juan, N.A.; Thomson, M.J. Simulating yield and morphology of carbonaceous nanoparticles during fuel pyrolysis in laminar flow reactors enabled by reactive inception and aromatic adsorption. *Combust. Flame* **2022**, *237*, 111721. [CrossRef]

Disclaimer/Publisher's Note: The statements, opinions and data contained in all publications are solely those of the individual author(s) and contributor(s) and not of MDPI and/or the editor(s). MDPI and/or the editor(s) disclaim responsibility for any injury to people or property resulting from any ideas, methods, instructions or products referred to in the content.